Journal of Colloid and Interface Science 602 (2021) 291–299

Contents lists available at ScienceDirect

Journal of Colloid and Interface Science

journal homepage: www.elsevier.com/locate/jcis

Regular Article

Nanonewton scale adhesion force measurements on biotinylated microbeads with a robotic micropipette

Rita Ungai-Salánki [a,b], Benjamin Csippa [c], Tamás Gerecsei [a,d], Beatrix Péter [d], Robert Horvath [d], Bálint Szabó [a,b,*]

[a] ELTE Eötvös Loránd University, Department of Biological Physics, Budapest, Hungary
[b] CellSorter Company for Innovations, Erdőalja út 174, H-1037 Budapest, Hungary
[c] Budapest University of Technology and Economics, Department of Hydrodynamic System, Budapest, Hungary
[d] Nanobiosensorics Laboratory, ELKH, Institute for Technical Physics and Materials Science, Centre for Energy Research, Budapest, Hungary

GRAPHICAL ABSTRACT

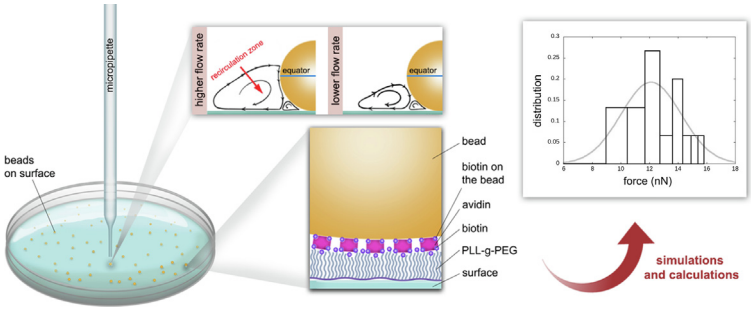

ARTICLE INFO

Article history:
Received 26 February 2021
Revised 26 May 2021
Accepted 31 May 2021
Available online 3 June 2021

Keywords:
Adhesion force
Binding force
Microbead
Micropipette
Computational fluid dynamics

ABSTRACT

Binding force between biomolecules has a crucial role in most biological processes. Receptor-ligand interactions transmit physical forces and signals simultaneously. Previously, we employed a robotic micropipette both in live cell and microbead adhesion studies to explore the adhesion force of biomolecules such as cell surface receptors including specific integrins on immune cells. Here we apply standard computational fluid dynamics simulations to reveal the detailed physical background of the flow generated by the micropipette when probing microbead adhesion on functionalized surfaces. Measuring the aspiration pressure needed to pick up the biotinylated 10 μm beads on avidin coated surfaces and converting it to a hydrodynamic lifting force on the basis of simulations, we found an unbinding force of 12 ± 2 nN, when targeting the beads manually; robotic targeting resulted in 9 ± 4 nN (mean ± SD). We measured and simulated the effect of the targeting offset, when the microbead was out of the axis (off-axis)of the micropipette. According to the simulations, the higher offset resulted in a higher lifting force acting on the bead. Considering this effect, we could readily correct the impact of the targeting offset to renormalize the experimental data. Horizontal force and torque also appeared in simulations in case of a targeting offset. Surprisingly, simulations show that the lifting force acting on the bead reaches a maximum at a flow rate of ~ 5 μl/s if the targeting offset is not very high (<5 μm). Further increasing the flow rate decreases the lifting force. We attribute this effect to the spherical geometry of the bead. We predict that higher flow rates cannot increase the hydrodynamic lifting force acting on the precisely targeted microbead, setting a fundamental force limit (16 nN in our setup) for manipulating microbeads with a

* Corresponding author at: ELTE Eötvös Loránd University, Department of Biological Physics, Budapest, Hungary.
E-mail address: balint.szabo@ttk.elte.hu (B. Szabó).

https://doi.org/10.1016/j.jcis.2021.05.180

micropipette perpendicular to the supporting surface. In order to extend the force range, we propose the offset targeting of microbeads.

1. Introduction

The noncovalent bond between the small organic molecule biotin (vitamin B7) and the 66 kDa protein avidin provides a well-known biochemical immobilization technique as both biotin and avidin can be easily conjugated to various molecules and surfaces [1]. The interaction between biotin and streptavidin (or avidin) are among the strongest protein–ligand interactions [2] with high affinity and specificity. To functionalize a plastic or glass microbead with a specific biomolecule like biotin and a planar surface with the partner molecule (avidin) for the characterization of the binding/adhesion force between them is a widespread method. This experimental setup can provide valuable information on colloidal systems, as well. Examples include particle aggregation and deposition [3], suspension rheology, and adhesion processes [4,5]. Techniques to characterize the binding force between microbeads and planar surfaces have emerged in the last decades. Centrifuge based methods [6,7], optical tweezers [8], biomembrane force probe (BFP) [2,9], and acoustic force spectroscopy (AFS) [10–13] were successfully utilized to probe this interaction. Shear-flow-induced detachment experiments combined with a theoretical model (based on the balance of hydrodynamic forces and torque exerted on microbeads) could determine the maximal adhesion force of BSA-coated microbeads to be 27.6 ± 8.5 nN [14].

However, the gold standard for such measurements is the atomic force microscope (AFM) [2,15–17]. By varying the loading rate (the speed of force exertion while pulling the microbead) the energy landscape of noncovalent bonds can be mapped. Rico et al. [18] determined the binding strength and unbinding pathways of the single avidin–biotin bond [19]. The dynamic force spectrum of the biotin-streptavidin bond was reported by Lo et al. [2]. Consistent with a BFP study by Evans [9], the dynamic force spectrum exhibited a linear relationship between the unbinding force and the logarithm of the loading rate. The colloid probe technique investigates the interaction force between single colloid particles and a substrate [20–22]. A spherical colloid is attached to a tipless AFM cantilever and used in force spectroscopic measurements [23,24]. Colloid based AFM can measure forces in the pN-nN range [25]. The fluidic force microscopy (FluidFM) [26,27] is a specialized AFM with a microfluidic channel inside the tip and the cantilever [25]. It provides an increased throughput for microbead force spectroscopy as compared to conventional AFM [25,28]. Previously, we measured the detachment force curve of biotinylated microbeads on an avidin coated surface with robotic fluidic force microscopy (FluidFM BOT) [28].

The computer-controlled robotic micropipette [29–34] is a straightforward tool to quantify the adhesion of live cells or functionalized microparticles. It can measure the adhesion strength of individual cells or microbeads with a relatively high throughput (hundreds of cells/beads in 30 min).

A glass micropipette is positioned above the bead recognized by computer vision and selected for measurement. Then an aspiration pressure is applied in the micropipette generating an inward fluid flow for a prescribed duration of typically 20–100 ms. By repeating the process with a stepwise increasing aspiration pressure and observing when the targeted bead is picked up, the unbinding pressure is determined for each bead. However, to precisely calculate the hydrodynamic lifting force acting on the bead, numerical simulations of the flow inside the micropipette and in the vicinity of the microbead are needed. For live cells, we completed similar computational fluid dynamics (CFD) simulations earlier [30,35]. However, both the morphology and biomechanics of live cells can be very complex, thus in the current study we used plastic microbeads as a simple model system. We constructed CFD simulations to calculate the precise hydrodynamic forces acting on microbeads. Using a robotic micropipette we measured the detachment of biotinylated polystyrene microbeads (d = 10 μm) from an avidin coated glass surface [28]. Our goal was to calculate the hydrodynamic lifting force acting on the targeted bead to precisely determine the unbinding (adhesion) force. In case of live cells such a calculation is challenging due to the variability in cell morphology and the complex viscoelastic behavior of the cytoskeleton. We investigated the effect of the bead targeting offset on the hydrodynamic lifting force, and calculated the horizontal force and torque acting on beads.

2. Materials and methods

2.1. Numerical simulations

Computational fluid dynamics (CFD) simulation was employed to calculate the lifting force and torque acting on a microbead in different flow conditions and micropipette positions. Numerical simulations were carried out with the ANSYS software package using the ANSYS CFX solver. The solver utilizes a coupled finite volume method to solve the underlying governing equations. These are the continuity, the Navier-Stokes and additional turbulence model equations. In the current study we used a similar workflow to that of our previous work [30]. The simulated fluid was water at the reference temperature of 25 °C. The material properties of density and dynamic viscosity were set to 997 kg/m^3 and 0.89 mPa*s, respectively. The flow was assumed to be laminar and no turbulence modeling was applied as the Reynolds number calculated with a reference length of the pipette tip diameter never reached more than 500.

The simulated geometry and its dimensions are depicted in Fig. 2. Due to meshing purposes, the microbead was floating 0.1 μm above from the bottom of the Petri dish, which is considered to be a good approximation of the bead sitting on the surface and has no additional effect on the emerging flow field. The tip of the pipette was positioned 10 μm above the bottom of the Petri dish according to the experimental protocol. To calculate the effect of the targeting error of the micropipette, the bead was offset by 5, 10 and 15 μm from the axis of the micropipette. Unstructured meshes consisting of tetrahedral and prismatic elements were created for all four scenarios. The mesh has to cover multiple scales of geometric dimensions from the size of the whole domain down to the size of the close vicinity of the bead itself. Thus, for the mesh to be applicable, especially at the tip of the pipette, a cascade of resolution criteria was set up growing outward from the microbead. Each mesh consisted of ~ 22 million numerical cells. Mesh independence study carried out to investigate the accuracy of simulations shows that this high-resolution mesh produced accurate results (Suppl. Table 2).

No-slip wall boundary condition was imposed on the bottom of the Petri dish, the microbead surface and on the wall of the glass micropipette. Although, it is known that the no-slip boundary condition is not perfect in microfluidic simulations [36–42], the so-

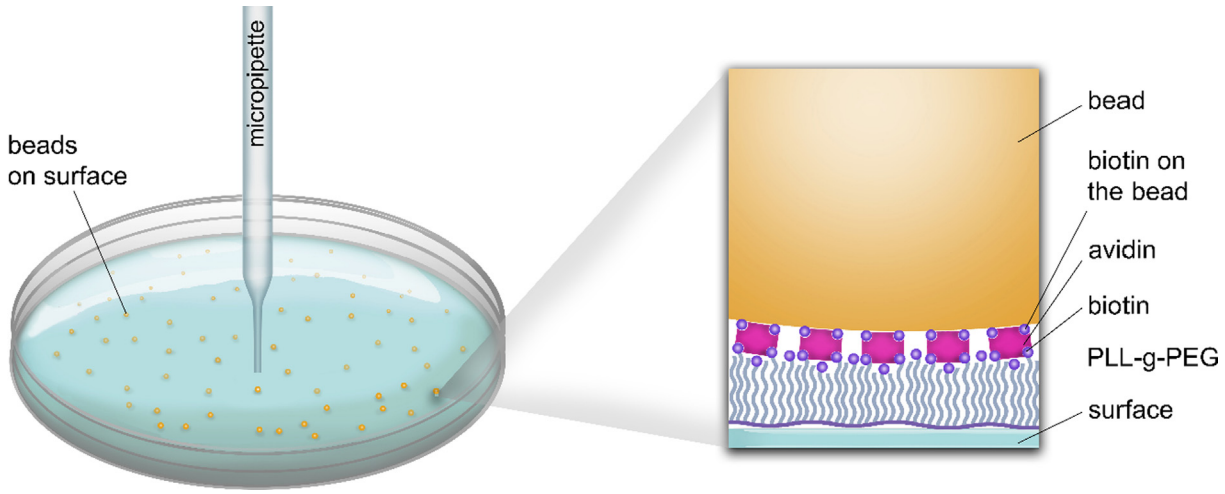

Fig. 1. Adhesion force measurement of functionalized microbeads attached to a planar surface using a micropipette. Masking non-specific interactions by the protein-repelling PLL-g-PEG coating is a simple and effective method. We used biotin-decorated PLL-g-PEG to achieve an adhesion generated by specific biotin-avidin binding. Beads were functionalized by biotin to attach to the remaining vacant binding sites on avidin.

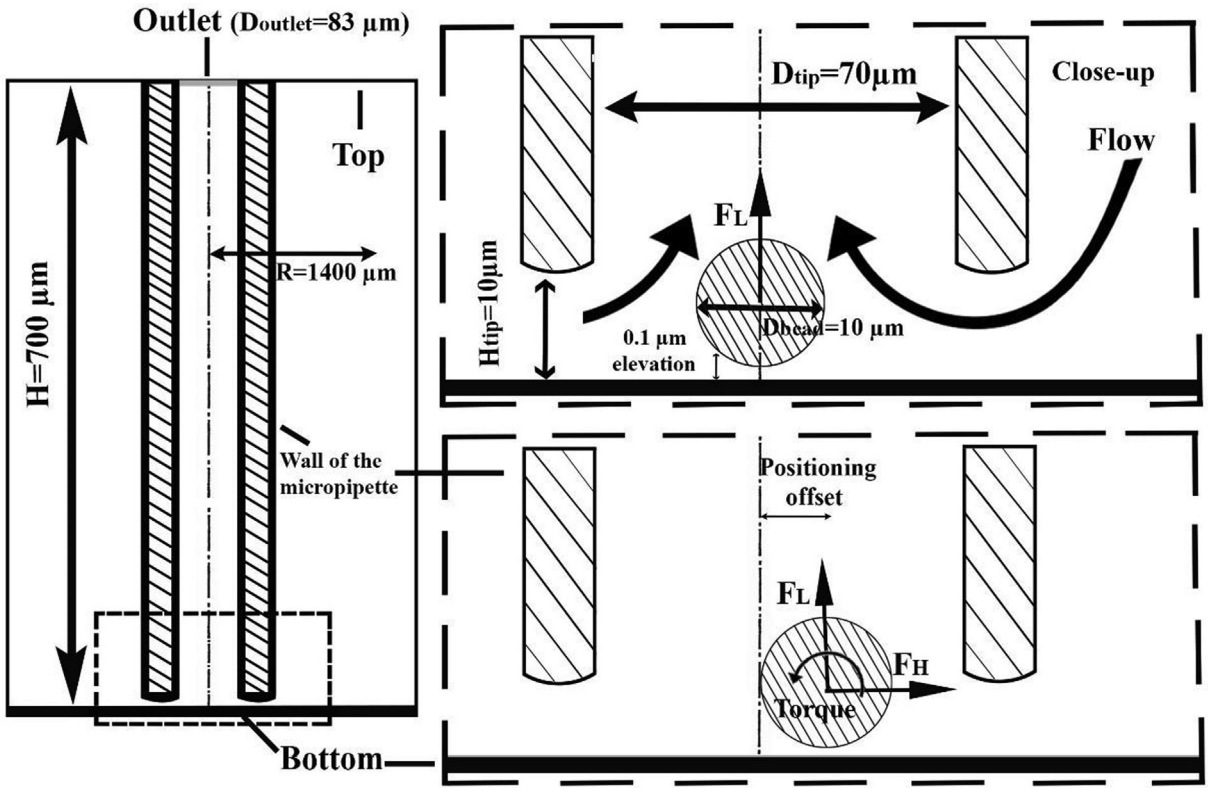

Fig. 2. Geometry of CFD simulations. A microbead (d = 10 µm) is floating 0.1 µm from above the bottom of the Petri dish. The tip of the micropipette is positioned h = 10 µm from the surface. To calculate the effect of misplacement of the micropipette on the lifting force, horizontal force and torque, the bead was offset in the middle of the micropipette (top right) and 5 µm; 10 µm (below right) and 15 µm distance from the center position of the micropipette.

called "slipping depth" is on the scale of water molecules being orders of magnitude lower than the dimensions of our microfluidic setup. Hence, we restricted ourselves to use the no-slip boundary condition. The outflow rate was prescribed on the upper opening of the micropipette called outlet. In the experiments, the aspiration pressure was set in the syringe connected to the micropipette with a long flexible PTFE tube. Therefore, the pressure in the micropipette was not an easily accessible experimental parameter. Thus, we measured the calibration curve between the flow rate and the aspiration pressure and used the flow rate as an input parameter for the CFD simulations. Flow rate was set to a value ranging from 1 to 10 µl/s at 1 µl/s increments. Each solution of the simulation was monitored by the numerical residuals and two physical quantities: the lifting force acting on the bead and the emerging pressure measured at the outlet. Simulation was stopped when the physical quantities reached a constant value and the residuals became lower than the criteria of 10^{-6}. Subsequently, the results were exported for post-processing in the open source software, ParaView to calculate the lifting force, the horizontal force, and the torque acting on the microbead.

2.2. Flow measurements in the micropipette

The glass micropipette connected to a syringe with a PTFE tube (I.D. 0.5 mm, length ~ 3 m) and a normally closed fluidic valve was filled with deionized water. Tubes and the valve were all filled with water, the syringe was filled with air [30]. We measured the weight of a 35 mm plastic Petri dish (hydrophobic, Greiner) with its lid on containing 3 ml deionized water on a laboratory scale. We positioned the tip of the I.D. 70 μm glass micropipette to a height of 10 μm above the surface of the Petri dish. To generate decreased pressure inside the syringe, the fluidic valve was kept closed, and the volume of the syringe was increased from an initial value of 40 ml to a higher value. After that, the fluidic valve was opened for a duration of 20 s to minimize transient effects. During this time, water entered the syringe, however the volume difference caused, did not exceed 1% in any of the measurements. The time that the Petri dish spent with its lid off was measured with a stopwatch. To calculate the flow rate at a given aspiration pressure after opening the valve, the weight of the Petri dish was measured again. The mass difference between the two measurements (Δm) is due to the water flow caused by the suction in the micropipette and the evaporation of the water during the measurement. The latter was corrected for by determining the evaporation rate from the Petri dish (with lid off) to be 0.035 mg/s. Evaporation with the lid on was measured to be quasi zero in five minutes. By multiplying the evaporation rate with the lid-off time, we could determine the mass lost due to the evaporation. All flow measurements were repeated three times.

2.3. Functionalized beads and surfaces

All chemicals used were analytical grade unless otherwise stated. 4-(2-hydroxyethyl)–1 piperazine ethanesulfonic acid (HEPES) assay buffer from Merck (Germany) was dissolved in Milli-Q water (with resistivity of 18 MΩ cm) to 10 mM and set to pH 7.4. The biotinylated synthetic copolymer, poly(Llysine)-*graft*-poly (ethylene glycol) (PLL-g-PEG), with the architecture of PLL(20)-g[3.5]-PEG(2)/PEG(3.4)-biotin with 50% of sidechains biotinylated was obtained in its powder form from SuSoS AG (Switzerland). The molecular weight of the PLL backbone and the PEG chains were 20 kDa and 2 kDa respectively and the grafting density [(lysine-mers)/(PEG side chains)] was 3.4. Avidin from egg white was purchased from VWR (Hungary) and aliquots were stored at 20 °C until use. 0.25 mg/ml avidin was dissolved in 10 mM HEPES buffer at pH 7.4 and applied in the experiments. Polystyrene biotinylated bead solution was purchased from Nanocs (USA) with an average bead diameter of d = 10 μm and a solid concentration of 1% and stored at 4 °C until use. To coat the Petri dish, 0.5 mg/ml PLL-g-PEG-biotin dissolved in 10 mM HEPES was pipetted and incubated on a rocker for 30 min at room temperature. Afterwards, the surface was washed three times with HEPES buffer and avidin solution (0.25 mg/ml in 10 mM HEPES) was added to the dish and incubated on a rocker for 30 min at room temperature. Subsequently, the dish was washed three times with HEPES buffer again. Then the bead solution (1 μl 1% bead stock solution in 1 ml HEPES) was pipetted into the dish and incubated on the microscope stage for 30 min before the adhesion measurement. Due to the protein-repellent properties of the PLL-g-PEG surface, non-specific adsorption was undetectable [28].

We estimated the surface density of biotin molecules on the bottom of the Petri dish based on [43]. From the physical parameters of the PLL-g-PEG grafted polymers, we acquired a surface number density of $\nu = 0.186\ 1/nm^2$ for biotin. Approximating the area of an avidin molecule by 5.6 nm × 5 nm [44] we estimate that each avidin has 5 possible biotin binding partners in the polymer layer. Furthermore, from previous measurements using label-free biosensors we determined that the number of avidin–biotin bonds anchoring a bead to the surface is approximately 100 [28]. The unbinding force of such an ensemble depends on the applied loading rate, as well as the single-bond rupture force in a nonlinear way discussed elsewhere [28,45].

2.4. Imaging and bead detection

The Petri dish was placed onto the sample holder insert (CellSorter) of the motorized inverted microscope (Zeiss Axio Observer A1). Then the region of interest (ROI) of the sample was scanned by a digital camera (Blackfly S) in bright field mode. The scanned image was analyzed by the CellSorter software and the beads were automatically detected using a built-in algorithm. To avoid picking up more than one bead per measurement, we excluded beads from the experiment when having neighbors in the close proximity (70 μm). The glass micropipette with an aperture of 70 μm approached the bottom of the Petri dish to a distance of 10 ± 1 μm.

2.5. Adhesion force measurement using manual targeting

To investigate the effect of the targeting offset, the beads were manually positioned into the axis (center) of the micropipette or to a horizontal offset of [0–20] μm from the axis of the micropipette using a 3D motorized micromanipulator (Marzhauser). In the beginning of the experiment we touched the surface of the Petri dish with the tip of the micropipette to calibrate its vertical position, then the height of the micropipette tip was adjusted to 10 ± 1 μm above the surface. The glass micropipette was connected to a 50 ml syringe with an inner diameter 0.5 mm PTFE tube. We controlled the flow with a high speed normally closed fluidic valve between the micropipette and the syringe. The entire fluidic system was filled with deionized water except the syringe. Aspiration pressure in the syringe filled with air was adjusted and the fluidic valve was opened for 100 ms [28,30]. If the bead was picked up, we turned to the next bead. If the bead remained on the surface, we increased the aspiration pressure. Aspiration pressure in the range of [6.9–23] kPa was increased in steps as long as the targeted bead was removed. Total number of beads probed by manual targeting was n = 58 in two experiments.

2.6. Automated adhesion force measurement using automated (adaptive) targeting

To achieve precise bead targeting we used an algorithm called adaptive targeting [46] to correct the coordinates of the bead right before probing it with the micropipette. Aspiration pressure in the range of [6.9–22] kPa was generated in the syringe using a syringe pump. After positioning the micropipette above a bead, the valve was opened for 100 ms to apply an aspiration pressure in the micropipette. After each cycle of the measurement the ROI was scanned again, and the aspiration pressure was increased to the next level. Subsequently, each redetected bead was probed again by the micropipette. CellSorter software determined the coordinates of the beads by computer vision and saved them before and after each cycle. Bead coordinates before and after each cycle were compared to determine automatically which beads were picked up. Total number of beads probed by the micropipette with adaptive targeting was n = 164 in two separate experiments.

2.7. Statistical analysis

All adhesion data shown in the figures were analyzed by the two-sample unpaired (one-tailed) *t*-test for comparing samples with 95% confidence.

3. Results

3.1. Numerical simulations

To calculate the hydrodynamic lifting force as a function of the experimental aspiration pressure and analyze the effect of the targeting offset on it, we ran 3D CFD simulations. We also calculated the horizontal force and torque acting on the beads in an offset position. We constructed a simple realistic geometry to model the glass micropipette and the polystyrene microbead (Fig. 2). Computations were run at 10 μm pipette height corresponding to the experimental conditions. To calculate the effect of the targeting offset of the micropipette, the bead was horizontally shifted by 5, 10 and 15 μm from the axis of the micropipette.

Result of the CFD simulations is summarized in Fig. 3. Pressure of the fluid and the wall shear stress on the surface of the bead are shown in two different color codes. Fluid velocity field is represented by the light arrows. Targeting offset results in a clear asymmetry of the pressure, wall shear stress and the flow velocity fields in the vicinity of the bead. A so-called 'recirculation zone' resides under the equator of the bead at every flow rate in the simulation. The reattachment line of this recirculation zone is the stagnation curve of the flow on the bead, where the Wall Shear Stress (WSS) is zero. The stagnation line can be visualized by plotting the WSS vector field marked with black arrows on the bead in Fig. 3. When the bead was in the center (axis) of the micropipette, the stagnation curve was at a certain latitude of the spherical bead. While in case of a low flow rate of 2 μl/s, this latitude was under the equator of the bead, it was above the equator in case of flow rates higher than 7 μl/s (Fig. 4).

We calculated the lifting force, horizontal force, and torque acting on the bead as a function of the flow rate in the range of [1;10] μl/s at 1 μl/s increments. Simulated results of the hydrodynamic lifting force (F_L) versus the flow rate (Q) were fitted by cubic polynomial functions. We calculated the three coefficients of this function and summarized them in Table 1. When the bead was in the axis of the micropipette or at 5 μm offset from it, the curves of the lifting force as a function of the flow rate had a very similar course (Fig. 5A). Surprisingly, in these cases, the hydrodynamic lifting force showed a decrease above 5 μl /s as a function of the flow rate. Even in case of 10 μm offset, the curve of the lifting force reached its maximum at 7 μl /s.

3.2. Bead adhesion force measurement with manual bead targeting

Using the micropipette setup, we measured the aspiration pressure needed to remove the surface attached microbeads by targeting them manually on the microscope. Our goal was to experimentally determine the effect of the targeting offset on the hydrodynamic lifting force (Fig. 5). The bead was positioned into the center (axis) of the micropipette or to a 5, 10, 15 or 20 μm horizontal offset from that (Figs. 1–2). The higher targeting offset resulted in lower aspiration pressure required to detach the beads from the surface. We classified the experiments into 4 groups based on the targeting offset (*TO*) as follows: *TO* < 5 μm, 5 μm <=*TO* < 10 μm, 10 μm <= *TO* < 15 μm, 15 μm <=*TO* < 20 μm (Fig. 6). Bead detachment results were plotted as a function of the experimental aspiration pressure in the case of *TO* < 5 μm and fitted by a Gaussian curve (Fig. 6C).

We found that the beads detached from the surface at an average aspiration pressure of 0.146 ± 0.01 atm, when the targeting offset was<5 μm (Fig. 6B). The result was very similar in case of 5 μm <=*TO* < 10 μm. We observed a significantly lower aspiration pres-

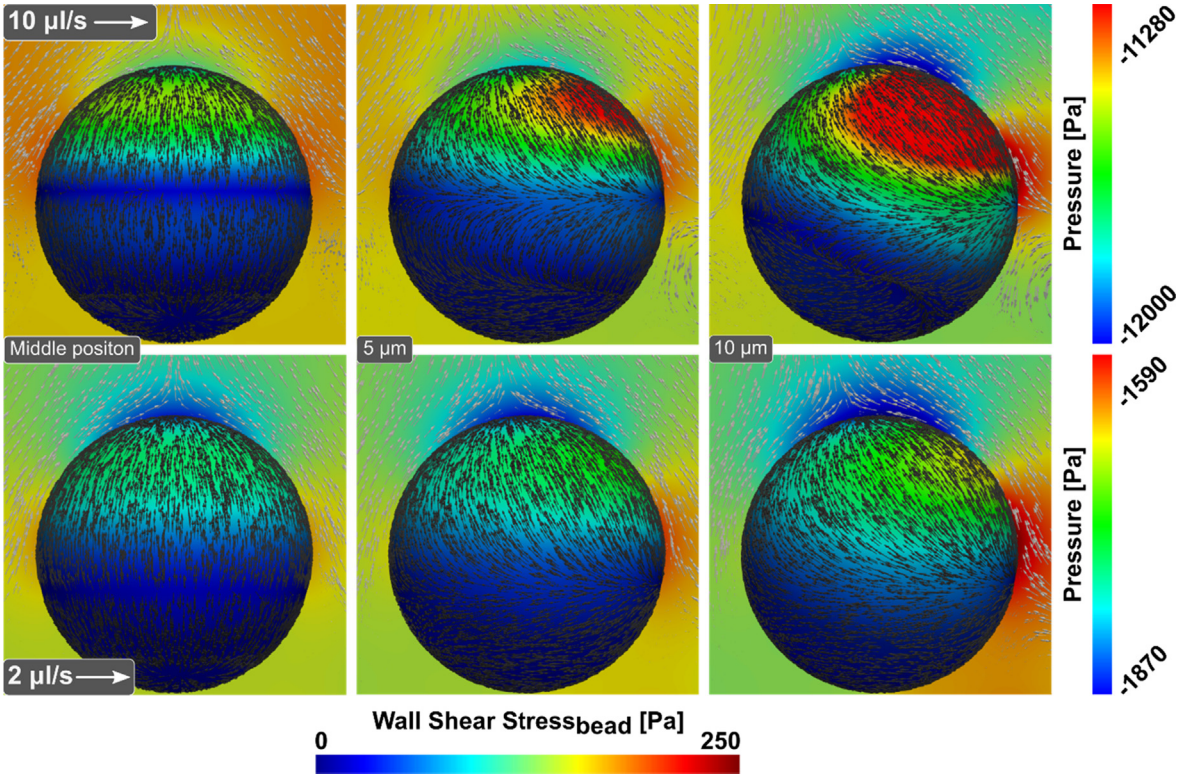

Fig. 3. Result of the CFD simulations. Comparison of the simulated flow generated by micropipette suction at flow rates of 2 and 10 μl/s. Th bead was in the axis of the micropipette or at 5 or 10 μm offset from that. Distance between the tip of the micropipette and the bottom of the Petri dish was 10 μm. Pressure of the fluid and the wall shear stress on the surface of the bead are shown in two different color codes. Fluid velocity field is represented by the light arrows. Wall Shear Stress (WSS) vector field is marked with black arrows on the bead surface. Targeting offset results in a clear asymmetry of the pressure, wall shear stress and the flow velocity fields in the vicinity of the bead.

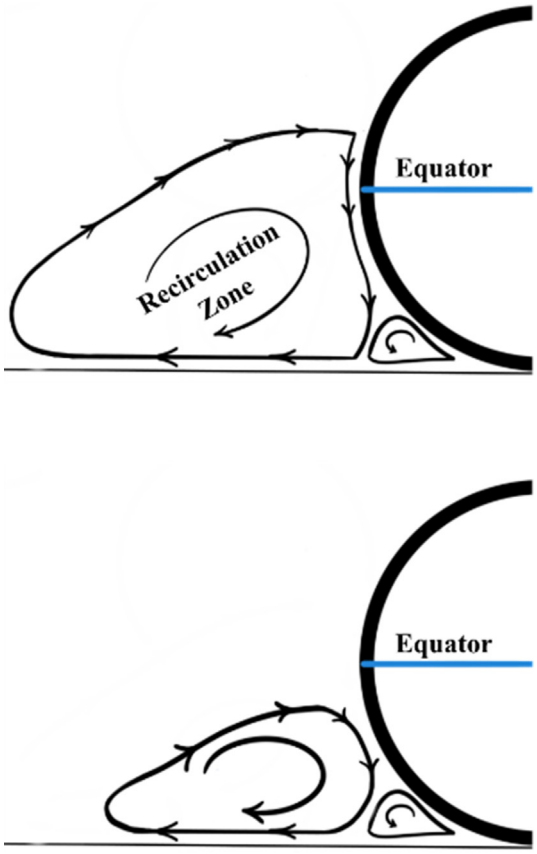

Fig. 4. Recirculation zone beside the microbead. When the bead was in the axis of the micropipette, the stagnation curve was at a certain latitude of the spherical bead. While in case of a flow rate higher than 7 μl/s this latitude was above the equator of the bead (upper drawing), in case of a lower flow rates, this latitude was under the equator (lower drawing).

sure needed to detach the beads when the targeting offset was higher than 10 μm.

We converted the experimental aspiration pressure in the syringe to a hydrodynamic lifting force in two steps based on an experimental calibration line (**Suppl.** Fig. 1) and on computer simulations of the flow in the micropipette (Fig. 5A, Table 1). This calculation resulted in a plot (Fig. 6D) showing the same lifting force needed to detach the beads for all 3 groups with a targeting offset<15 μm. However, experimental results measured at higher than 15 μm targeting offset show deviation from the other three groups.

10 beads in the range of 0–5 μm targeting offset and 1 bead in the range of 5–10 μm targeting offset did not detach from the surface even under the highest aspiration pressure (23 kPa) we applied. These beads are not shown in Fig. 6.

3.3. Adhesion force measurement using automated (adaptive) targeting

To achieve proper robotic bead targeting, we used the adaptive targeting [46] algorithm of the CellSorter software. After completing the initial scan of the entire sample (all beads to be probed), the algorithm captures a new image before targeting the next bead with the micropipette, locates the bead in the image and corrects its horizontal coordinates. This method eliminates most of the inaccuracy of the XY motorized stage and corrects any displacement of the bead that happened after the initial scan. We found that the beads detached from the surface at an average aspiration pressure of 0.105 ± 0.033 atm based on the fitted Gaussian distribution (Fig. 7). 44 out of the 164 beads remained on the surface even after applying the highest aspiration pressure (22 kPa) we

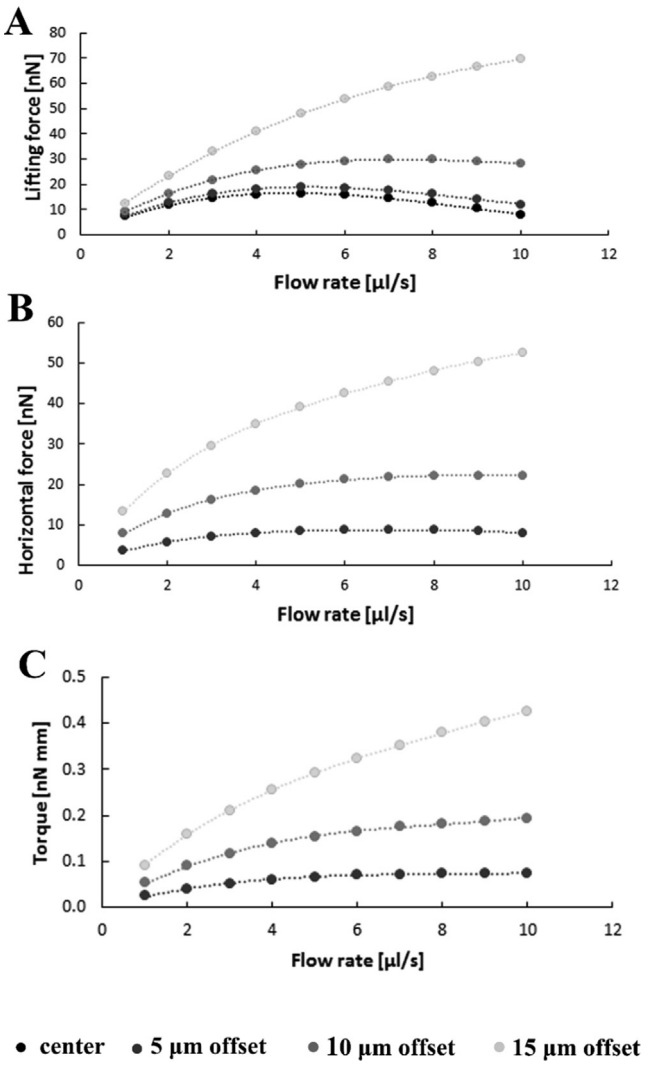

Fig. 5. On the basis of the simulations, the lifting force (top), horizontal force (middle) and torque (bottom) acting on the bead was determined as a function of the flow rate in the range of [1;10] μl/s at 1 μl/s increments. Simulated results of the hydrodynamic lifting force (F_L), horizontal force, and torque versus the flow rate (Q) were fitted by cubic polynomial functions. This was the simplest model properly fitting the simulated data. **(A, B, C)** coefficients of the $F_L = A^*Q^3 + B^*Q^2 + C^*Q$ were calculated in case of the four different positions of the bead and summarized in Table 1.

Table 1
Hydrodynamic lifting force (F_L) as a function of the flow rate (Q) fitted by a cubic polynomial function. Table shows the (A, B, C) coefficients of the cubic polynomial function of $F_L = A^*Q^3 + B^*Q^2 + C^*Q$ in case of the four different bead positions. We used these coefficients to convert the experimental flow rate values to an estimated lifting force.

Bead targeting	A [nN/(μl/s)^3]	B [nN/(μl/s)^2]	C [nN/(μl/s)]	R^2
center	0.0422	−1.1315	7.9198	0.9913
5 μm offset	0.0428	−1.1586	8.5273	0.9946
10 μm offset	0.0391	−1.1403	10.333	0.9997
15 μm offset	0.0232	−0.8701	13.346	1

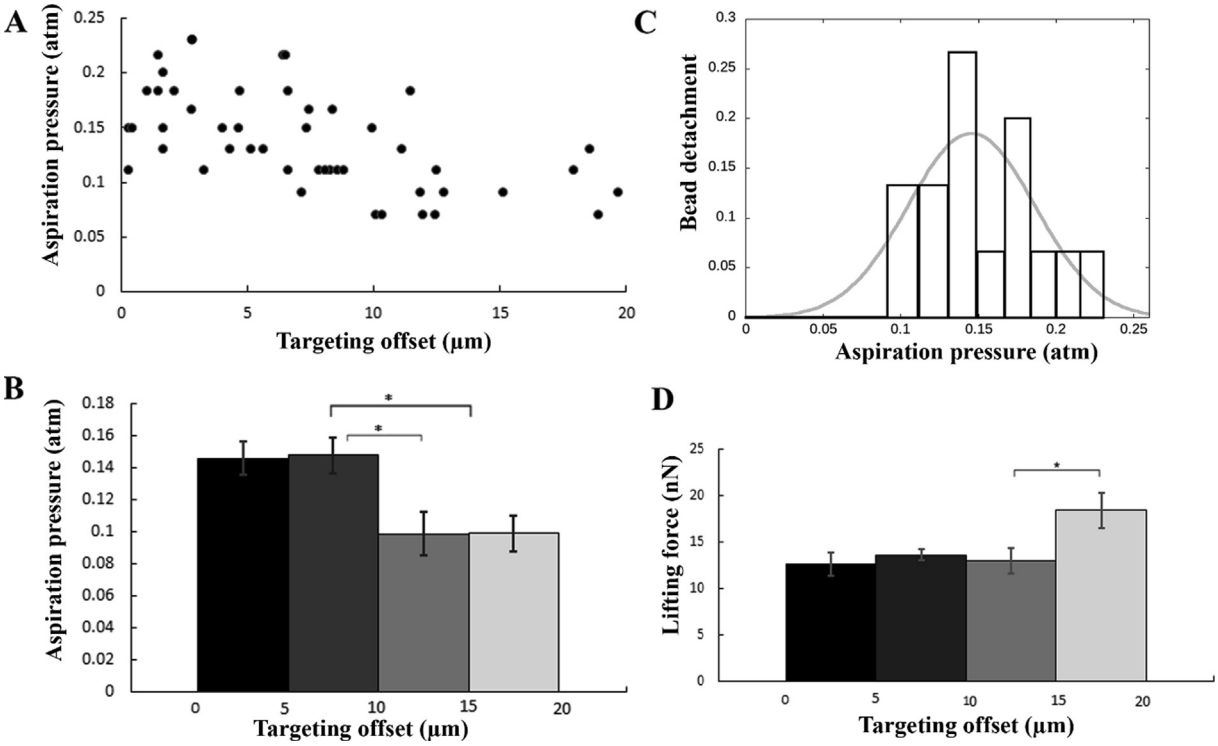

Fig. 6. Experimental microbead detachment data gained with manual bead targeting. **A)** Aspiration pressure needed to detach the beads as a function of the targeting offset. 10 beads in the range of 0–5 μm targeting offset and 1 bead in the range of 5–10 μm targeting offset did not detach from the surface even under the highest aspiration pressure we used. These beads are not shown in the plots. **B)** Results were divided into 4 groups based on the targeting offset. **C)** Distribution of bead detachments as a function of the aspiration pressure when the accuracy of the targeting was better than 5 μm. We fitted a Gaussian curve to the data. The peak of the Gaussian curve was at 0.146 ± 0.01 atm with a distribution standard deviation of 0.04 ± 0.011 atm. RMS of the residuals is 0.0602. **D)** Experimental aspiration pressure was converted to a hydrodynamic lifting force in two steps based on the calibration line (**Suppl**. Fig. 1) and on computer simulations of the flow in the micropipette (Fig. 5**A,** Table 1). * indicates significant difference between the groups ($p < 0.05$).

used. The average targeting offset was 1.7 ± 0.1 μm with automated targeting.

3.4. Adhesion force of microbeads

We calculated the adhesion force distribution of the beads using the experimental results and simulations (Fig. 8). We compared the result of manual and automated bead targeting. We acquired the distribution of bead adhesion force by first converting the aspiration pressure to flow rate based on the calibration line (**Suppl.** Fig. 1), and then calculating the hydrodynamic lifting force according to simulations (Fig. 5**A,** Table 1). Distributions were fitted with Gaussian curves. Mean and standard deviation of the fitted Gaussian distributions are shown in Table 2.

Fitting the Gaussian curve to the experimental bead detachment distribution first (as shown in Fig. 6C and Fig. 7**)**, and then converting the mean and standard deviation of the Gaussian distribution applying the calibration line (**Suppl**. Fig 1.) results in similar values but higher standard errors (**Suppl**. Table 1).

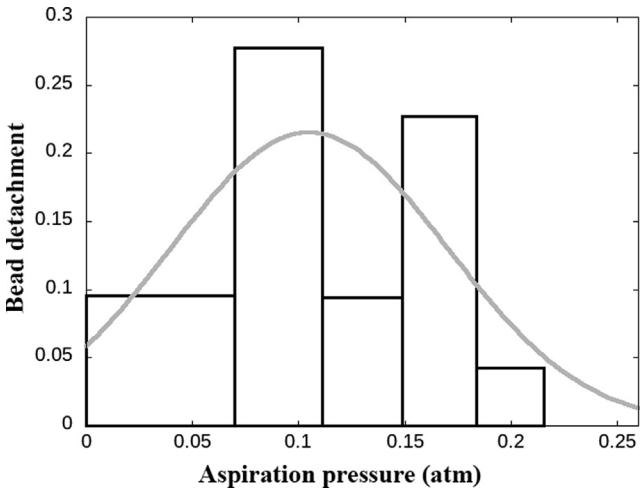

Fig. 7. Distribution of bead detachments as a function of the aspiration pressure applied in case of automated targeting. The micropipette targeted the center of the beads using adaptive targeting, an algorithm correcting the coordinates of the bead right before targeting. Data was fitted by a Gaussian curve. The peak of the curve was at 0.105 ± 0.033 atm with a distribution standard deviation of 0.06 ± 0.039 atm. RMS of the residuals is 0.107398.

4. Discussion

We applied standard computational fluid dynamics simulations to reveal the detailed physical background of the flow generated by the micropipette when probing microbead adhesion on a functionalized planar surface. Measuring the aspiration pressure needed to pick up biotinylated 10 μm size beads on avidin coated surfaces and converting the experimental aspiration pressure to a hydrodynamic lifting force on the basis of simulations, we found an unbinding force of 12 ± 2 nN, when targeting the beads manually. Robotic adaptive targeting resulted in 9 ± 4 nN (mean ± SD).

We measured and simulated the effect of the targeting offset, when the microbead was out of the axis of the micropipette. According to the simulations, the higher offset resulted in a higher

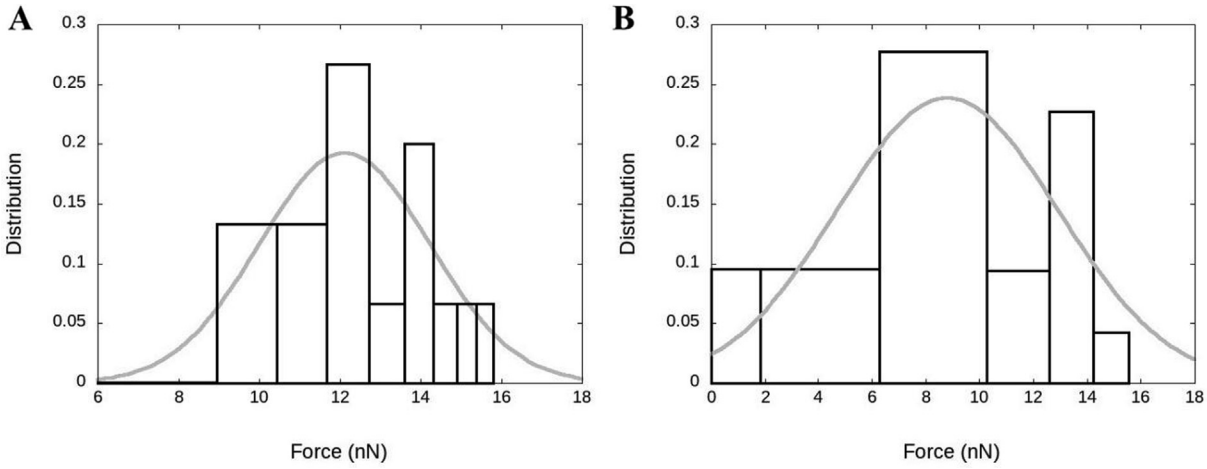

Fig. 8. Distributions of the microbead adhesion force measured by manual **(A)** and automated **(B)** targeting. Plots show the data collected by precise targeting, i.e., the targeting offset was<5 μm. First, we converted the aspiration pressure to flow rate based on the calibration line (**Suppl.** Fig. 1), and then calculated the hydrodynamic lifting force according to simulations (Fig. 5A, Table 1).

Table 2
We calculated and compared the resulting adhesion force measured by manual and automated targeting in case of precise targeting, i.e., targeting offset<5 μm.

Targeting method	Lifting force (nN)	Standard deviation (nN)
Manual	12.12 ± 0.5	1.91 ± 0.48
Automated	8.82 ± 1.87	4.11 ± 1.9

hydrodynamic lifting force acting on the bead. Considering this effect, we could readily correct the impact of the targeting offset to renormalize the experimental data.

Horizontal force and torque also appeared in simulations in case of a targeting offset. Surprisingly, simulations show that the lifting force acting on the bead reaches a maximum at a flow rate of ~ 5 μl/s if the targeting offset is not very high (<5 μm). Further increasing the flow rate decreases the lifting force. We attribute this effect to the spherical geometry of the bead. A so called 'separation bubble' appeared under the equator of the bead at every flow rate in the simulation. When the bead was in the center (axis) of the micropipette, the stagnation curve was at a certain latitude of the spherical bead. While in case of a low flow rate of 2 μl/s this latitude was under the equator of the bead, it was above the equator in case of flow rates higher than 7 μl/s. We think that this observation can explain why the lifting force acting on the bead becomes smaller at higher flow rates. In the experiments the flow rate is gradually building up in the micropipette and thus it is expected to lift the bead before this phenomenon occurs. However, we predict that higher than 5 μl/s flow rates cannot increase the hydrodynamic lifting force acting on the precisely targeted microbead setting a fundamental force limit for manipulating microbeads with a micropipette perpendicular to the planar surface holding the beads. In our setup this force limit was 16 nN. This limitation can be overcome by the offset targeting of microbeads.

Previously, we measured the adhesion force of the same system of biotinylated microbeads on the avidin coated surface with a specialized atomic force microscope (AFM): FluidFM [28] with a result of **37.5 ± 1.8 nN** (mean ± standard error of the mean). Considering that the detachment force measured by AFM strongly depends on the loading rate, and the aspiration pressure needed to pick up the beads with the micropipette also depends on the duration of the flow [28], we think that our new result of **12.12 ± 0.5 nN** (mean ± standard error of the mean) is in the reasonable range. Detachment force of smaller (3 μm) avidin-coated beads on the same PLL-g-PEG-biotin layer was measured to be **11 ± 1 nN** using FluidFM [25].

5. Conclusions

Our hypothesis was that by employing a pressure-controlled micropipette along with fluid dynamics simulations it is possible to measure the unbinding force of microbeads attached to a surface by specific biochemical bonds. Crucial element of our concept was that the spherical microbeads and the cylindrical micropipette above a planar surface result is a simple 3D geometry allowing repeatable experiments and straightforward simulations.

We determined an unbinding force of 12 ± 2 nN, when manually targeting the biotinylated 10 μm beads attached to the avidin coated surface with a vertical micropipette; robotic targeting resulted in 9 ± 4 nN (mean ± SD). Moreover, we showed that targeting offset, i.e., when the microbead is out of the center (axis) of the micropipette, results in a higher lifting force acting on the targeted bead. In this case horizontal force and torque also appeared in the simulations.

Today, the gold standard of nanonewton scale force measurements is the AFM [2,15,16,17]. A modified AFM, the fluidic force microscope (FluidFM) provides higher throughput by reversibly fixing the targeted bead on a hollow cantilever using vacuum, in contrast to irreversible chemical attachment on a traditional AFM cantilever [25,28]. Major advantage of our method - originally developed for picking single live cells - is its non-contact nature. The micropipette does not touch the microbead when probing the adhesion force allowing even higher throughput than FluidFM in a robotic setup. This non-contact nature minimizes the possible contamination of both the micropipette and the targeted bead especially useful for probing a large number of microbeads.

We expect that the micropipette-microbead based method introduced here will be applied to measure the detachment force of many more molecular interactions and will be widely employed to characterize the binding forces between surfaces. It is suitable for comparative studies, e.g., to investigate the effect of a specific drug or protein/ligand modifications on surface-to-surface interactions in a simple, automated, and high throughput manner.

CRediT authorship contribution statement

Rita Ungai-Salánki: Methodology, Investigation, Writing - original draft. **Benjamin Csippa:** Methodology, Investigation, Writing - original draft. **Tamás Gerecsei:** Conceptualization, Writing - review & editing. **Beatrix Péter:** Visualization. **Robert Horvath:** Conceptu-

alization, Writing - review & editing, Funding acquisition. **Bálint Szabó:** Conceptualization, Writing - original draft, Supervision.

Declaration of Competing Interest

Bálint Szabó is a founder of CellSorter Company for Innovations, Other authors declare that they have no known competing financial interests or personal relationships that could have appeared to influence the work reported in this paper.

Acknowledgements

This work was supported by the National Research, Development and Innovation Office (grant numbers: PD 124559 for R. U. S., PD 131543 for B. P., ERC_HU, KH_17, and KKP_19 Programs for R. H.), the Hungarian Academy of Sciences [Lendület (Momentum) Program] for R. H.

Appendix A. Supplementary material

Supplementary data to this article can be found online at https://doi.org/10.1016/j.jcis.2021.05.180.

References

[1] M. Wilchek, E.A. Bayer, O. Livnah, Essentials of biorecognition: The (strept) avidin-biotin system as a model for protein-protein and protein-ligand interaction, Immunol. Lett. 103 (2006) 27–32.
[2] Yu-Shiu Lo, Ying-Jie Zhu, P. Thomas, J. Beebe, Loading-Rate Dependence of Individual Ligand-Receptor Bond-Rupture Forces Studied by Atomic Force Microscopy, Langmuir 17 (2001) 3741–3748.
[3] M. Elimelech, J. Gregory, X. Jia, R. W. Particle Deposition and Aggregation: Measurement, Modelling and Simulation (1998).
[4] M.A.S. Quintanilla, A. Castellanos, J.M. Valverde, Correlation between bulk stresses and interparticle contact forces in fine powders. 64 (2001) 1–9.
[5] M. Holmberg, R. Wigren, R. Erlandsson, P.M. Claesson, Interactions between cellulose and colloidal silica in the presence of polyelectrolytes, Colloids Surfaces A Physicochem. Eng. Asp. 129–130 (1997) 175–183.
[6] F. Podczeck, J.M. Newton, M.B. James, Influence of relative humidity of storage air on the adhesion and autoadhesion of micronized particles to particulate and compacted powder surfaces, J. Colloid Interface Sci. 187 (1997) 484–491.
[7] Junlin Yang, Rolf Bos, Albert Poortinga, Poppo J. Wit, Gerald F. Belder, H. J. B. Comparison of Particle Deposition in a Parallel Plate and a Stagnation Point Flow Chamber. Langmuir 15 (1999), 4671–4677.
[8] K.C. Neuman, A. Nagy, Single-molecule force spectroscopy: optical tweezers, magnetic tweezers and atomic force microscopy, Nat. Methods 5 (2008) 491–505.
[9] R. Merkel, P. Nassoy, A. Leung, K. R. & E. E Energy landscapes of receptor–ligand bonds explored with dynamic force spectroscopy, Nature 397 (1999) 50–53.
[10] D. Kamsma, G.J.L. Wuite, Single-molecule measurements using acoustic force spectroscopy (AFS), Methods Mol. Biol. 1665 (2018) 341–351.
[11] G. Sitters et al., Acoustic force spectroscopy, Nat Methods. 12 (2014) 47–50.
[12] G. Bergamaschi, A. Biebricher, G.J.L. Wuite, From Nuclei to Artificial Cells: Probing the Mechanics of Minimal Systems, Biophys. J. 116 (2019) 123a.
[13] Margherita Marchetti, Douwe Kamsma, Ernesto Cazares Vargas, Armando Hernandez García, Paul van der Schoot, Renko de Vries, Gijs J. L. Wuite, and W. H. R. Real-Time Assembly of Viruslike Nucleocapsids Elucidated at the Single-Particle Level. Nano Lett. 19 (2019) 5746–5753.
[14] M. Mercier-Bonin et al., Evaluation of adhesion force between functionalized microbeads and protein-coated stainless steel using shear-flow-induced detachment, J. Colloid Interface Sci. 338 (2009) 73–81.
[15] E. Evans, Probing the relation between force - Lifetime - And chemistry in single molecular bonds, Annu. Rev. Biophys. Biomol. Struct 30 (2001) 105–128.
[16] G. Binnig, C.F. Quate, Atomic force microscope, Phys. Rev. Lett. 56 (1986) 930–933.
[17] M. De Odrowaz Piramowicz, P. Czuba, M. Targosz, K. Burda, M. Szymoński, Dynamic force measurements of avidin-biotin and streptavdin-biotin interactions using AFM. Acta Biochim. Pol. 53 (2006) 93–100.
[18] F. Rico, A. Russek, L. González, H. Grubmüller, S. Scheuring, Heterogeneous and rate-dependent streptavidin–biotin unbinding revealed by high-speed force spectroscopy and atomistic simulations, Proc. Natl. Acad. Sci. U. S. A. 116 (2019) 6594–6601.
[19] M. Benoit, H.E. Gaub, Measuring cell adhesion forces with the atomic force microscope at the molecular level, Cells Tissues Organs 172 (2002) 174–189.
[20] W.A. Ducker, T.J. Senden, R.M. Pashley, Direct measurement of colloidal forces using an atomic force microscope, Nature 353 (1991) 239–241.
[21] H.J. Butt, Measuring electrostatic, van der Waals, and hydration forces in electrolyte solutions with an atomic force microscope, Biophys. J. 60 (1991) 1438–1444.
[22] M. Kappl, H.J. Butt, The colloidal probe technique and its application to adhesion force measurements, Part. Part. Syst. Charact. 19 (2002) 129–143.
[23] N. Hilal, W.R. Bowen, L. Alkhatib, O. Ogunbiyi, A review of atomic force microscopy applied to cell interactions with membranes, Chem. Eng. Res. Des. 84 (2006) 282–292.
[24] P. Knittel, T. Yoshikawa, C.E. Nebel, Diamond colloidal probe force spectroscopy, Anal. Chem. 91 (2019) 5537–5541.
[25] P. Dörig et al., Exchangeable colloidal AFM probes for the quantification of irreversible and long-term interactions, Biophys. J. 105 (2013) 463–472.
[26] Nagy, Á. G., Kámán, J., Horváth, R. & Bonyár, A. Publisher Correction: Spring constant and sensitivity calibration of FluidFM micropipette cantilevers for force spectroscopy measurements (Scientific Reports, (2019), 9, 1, (10287), 10.1038/s41598-019-46691-x). Sci. Rep. 9, 1–11 (2019)
[27] N. Helfricht, Extending the limits of direct force measurements : colloidal probes from sub-micron particles, Nanoscale (2017).
[28] T. Gerecsei et al., Adhesion force measurements on functionalized microbeads: An in-depth comparison of computer controlled micropipette and fluidic force microscopy, J. Colloid Interface Sci. 555 (2019) 245–253.
[29] N. Sándor et al., CD11c / CD18 Dominates Adhesion of Human Monocytes, Macrophages and Dendritic Cells over CD11b / CD18, PLoS One 11 (2016) e0163120.
[30] R. Salánki et al., Single Cell Adhesion Assay Using Computer Controlled Micropipette, PLoS One 9 (2014) e111450.
[31] P.K. Jani et al., Complement MASP-1 enhances adhesion between endothelial cells and neutrophils by up-regulating E-selectin expression, Mol. Immunol. 75 (2016) 38–47.
[32] Ungai-Salánki, R. et al. A practical review on the measurement tools for cellular adhesion force. arXiv 1–81 (2019).
[33] S. Lukácsi et al., The differential role of CR3 (CD11b/CD18) and CR4 (CD11c/CD18) in the adherence, migration and podosome formation of human macrophages and dendritic cells under inflammatory conditions, PLoS One 15 (2020) 1–21.
[34] T. Gerecsei et al., Dissociation Constant of Integrin-RGD Binding in Live Cells from Automated Micropipette and Label-Free Optical Data, Biosensors 11 (2021) 1–11.
[35] Z. Környei et al., Cell sorting in a Petri dish controlled by computer vision, Sci. Rep. 3 (2013).
[36] Y. Zhu, S. Granick, Limits of the Hydrodynamic No-Slip Boundary Condition, Phys. Rev. Lett. (2002), https://doi.org/10.1103/PhysRevLett.88.106102.
[37] J. Xu, Y. Li, Boundary conditions at the solid-liquid surface over the multiscale channel size from nanometer to micron, Int. J. Heat Mass Transf. 50 (2007) 2571–2581.
[38] C. Neto, D.R. Evans, E. Bonaccurso, H.J. Butt, C. V Boundary slip in Newtonian liquids: a review of experimental studies. *Reports*, Prog. Phys. 68 (2005) 2859–2897.
[39] R.S. Voronov, D.V. Papavassiliou, L.L. Lee, Review of fluid slip over superhydrophobic surfaces and its dependence on the contact angle, Ind. Eng. Chem. Res. 47 (2008) 2455–2477.
[40] Y. Zhu, S. Granick, Rate-Dependent Slip of Newtonian Liquid at Smooth Surfaces, Phys. Rev. Lett. 87 (2001).
[41] D.C. Tretheway, C.D. Meinhart, A generating mechanism for apparent fluid slip in hydrophobic microchannels, Phys. Fluids 16 (2004) 1509–1515.
[42] E. Lauga, M.P. Brenner, H.A. Stone, Microfluidics : The No-Slip Boundary Condition. 1–27 (2005).
[43] N. Orgovan et al., Dependence of cancer cell adhesion kinetics on integrin ligand surface density measured by a high-throughput label-free resonant waveguide grating biosensor, Sci. Rep. 4 (2014) 4034.
[44] Luisa Pugliese;Alessandro Coda; Massimo Malcovati; Martino Bolognesi. Three-dimensional structure of the tetragonal crystal form of egg-white avidin in its functional complex with biotin at 2· 7 Å resolution. J. Mol. Biol. Vol. 23 (1993) 698–710.
[45] P.M. Williams, Analytical descriptions of dynamic force spectroscopy: behaviour of multiple connections, Anal. Chim. Acta 479 (2003) 107–115.
[46] R. Ungai-Salánki et al., Automated single cell isolation from suspension with computer vision, Sci. Rep. 6 (2016) 20375.